

# Nonequilibrium ionization states and cooling rates of the photoionized enriched gas

Evgenii O. Vasiliev<sup>1\*</sup>

<sup>1</sup>*Institute of Physics, Southern Federal University, Stachki Ave. 194, Rostov-on-Don, 344090 Russia*

Accepted 3004 December 15. Received 2004 December 14; in original form 2004 December 31

## ABSTRACT

Nonequilibrium (time-dependent) cooling rates and ionization state calculations are presented for low-density gas enriched with heavy elements (metals) and photoionized by external ultraviolet/X-ray radiation. We consider a wide range of gas densities and metallicities and also two types of external radiation field: a power-law and the extragalactic background spectra. We have found that both cooling efficiencies and ionic composition of enriched photoionized gas depend significantly on the gas metallicity and density, the flux amplitude, and the shape of ionizing radiation spectrum. The cooling rates and ionic composition of gas in nonequilibrium photoionization models differ strongly (by a factor of several) from those in photoequilibrium due to overionization of the ionic states in the nonequilibrium case. The difference is maximal at low values of the ionization parameter and similar in magnitude to that between the equilibrium and nonequilibrium cooling rates in the collisionally controlled gas. In general, the nonequilibrium effects are notable at  $T \lesssim 10^6$  K. In this temperature range, the mismatch of the ionic states and their ratios between the photoequilibrium and the photo-nonequilibrium models reach a factor of several. The net result is that the time-dependent energy losses due to each chemical element (i.e. the contributions to the total cooling rate) differ significantly from the photoequilibrium ones. We advocate the use of nonequilibrium cooling rates and ionic states for gas with near-solar (and above) metallicity exposed to an arbitrary ionizing radiation flux. We provide a parameter space (in terms of temperature, density, metallicity and ionizing radiation flux), where the nonequilibrium cooling rates are to be used. More quantitatively, the nonequilibrium collisional cooling rates and ionization states are a better choice for the ionization parameter  $\log U \lesssim -5$ . The difference between the photoequilibrium and the photo-nonequilibrium decreases with the ionization parameter growth, and the photoequilibrium can be used for ionization parameter as high as  $\log U \gtrsim -2$  for  $Z \lesssim 10^{-2}Z_{\odot}$  and  $\log U \gtrsim 0$  for  $Z \sim Z_{\odot}$ . Thus, the nonequilibrium calculations should be used for the ionization parameter range between the above-mentioned values. In general, where the physical conditions are favour to collisional ionization, the nonequilibrium (photo)ionization calculations should be conducted.

**Key words:** cosmology: theory – diffuse radiation – intergalactic medium – quasars: general – absorption lines – physical data and processes: atomic processes

## 1 INTRODUCTION

Recent observations of heavy elements (metals) in the intergalactic medium (IGM) give rich information about star formation and enrichment history of the Universe (Madau et al. 1996; Pettini 1999; Schaye et al. 2003; Nicastro et al. 2006; Simcoe et al. 2006; Danforth & Shull 2008). In order to understand these observations, it is nec-

essary to know which processes are responsible for the observed ionic composition and thermal state of the IGM. In the absence of ionizing background radiation, these processes are controlled by collisions and determined by gas metallicity and temperature. However, when galaxies and quasars form they produce strong ionizing photons (Haardt & Madau 1996, 2001; Miniati et al. 2004; Faucher-Giguère et al. 2009). Therefore photoionization and photoheating are to be taken into account.

Calculations of the cooling rates of astrophysical plasma

\* E-mail: eugstar@mail.ru

in the collisional ionization equilibrium (CIE) were performed by many authors (House 1964; Cox & Tucker 1969; Raymond et al. 1976; Shull & van Steenberg 1982; Gaetz & Salpeter 1983; Böhringer & Hensler 1989; Sutherland & Dopita 1993; Landi & Landini 1999; Benjamin et al. 2001; Bryans et al. 2006). However, calculations of the time-dependent ionization of metals and associated radiative cooling showed significant deviations from the CIE states (Kafatos 1973; Shapiro & Moore 1976; Edgar & Chevalier 1986; Schmutzler & Tscharnuter 1993; Sutherland & Dopita 1993; Gnat & Sternberg 2007). In some conditions, ionizing radiation can be important for the thermal and ionization states of primordial and enriched gas. Efstathiou (1992) showed that the presence of UV radiation can strongly suppress the cooling rate of primordial gas. In the photoionization equilibrium case, Wiersma et al. (2009) came to a similar conclusion for enriched gas exposed to the external ionizing radiation. It is obvious that ionizing radiation forces the ionic composition of gas to settle on to photoequilibrium. However, during transition from a pure collisional to a photoequilibrium case the nonequilibrium effects are expected to play a role.

In general, numerical simulations of metal ionization states in the IGM should take into account the effects of ionizing background. However, this requires tracing huge number of metal species and their ionization states, as well as complex calculations of the cooling and heating rates of the enriched photoionized gas. Therefore, simulations often consider either a limited number of metal ionization states or cooling rates of collisionally ionized gas. For instance, Raga et al. (1997) studied a radiative bow shock using a limited ionization and cooling network; Yoshikawa & Sasaki (2006) used the CIE cooling rates to study the ionic composition of a warm-hot intergalactic medium. Hughes & Singh (1994) presented a comprehensive nonequilibrium ionization analysis of the supernova remnant. Recently, self-consistent calculations were successfully performed in one-dimension. Gnat & Sternberg (2004) studied the metals photoionization structures of pressure-supported gas clouds in dark matter minihalos and lately Gnat & Sternberg (2009) considered the ionic composition of gas in post-shock cooling layers behind fast radiative shock waves. More recently, three-dimensional nonequilibrium modelling of the interstellar medium were performed by de Avillez & Breitschwerdt (2010a,b). They considered the evolution of the turbulent magnetized interstellar medium taking into account the time-dependent ionization of ten main chemical elements. Here, we study how nonequilibrium affects the ionic composition and cooling rates of an enriched photoionized gas and analyze a parameter space (i.e., temperature, density, metallicity, and ionizing radiation flux) where the nonequilibrium effects should be taken into account.

In the last decade studies of the intergalactic gas became very intensive. Among the most interesting are the conclusions about the total mass of baryons in the Universe and its metal fraction. Fukugita & Peebles (2004) have estimated the cosmic baryon budget and found that less than 10% of the total baryonic content in the Universe is locked in the form of collapsed objects (stars, galaxies, groups). More recently Danforth & Shull (2008) founded that approximately  $\sim 50\%$  of the baryons remain unaccounted for. A significant discrepancy is also established

for the total mass of metals observed in the Universe and the metal budget estimated from the total star formation rate. This lack of metals is known as the missing metals problem (Pettini 1999). Numerical simulations led by Cen & Ostriker (1999) suggest that approximately 30 to 50% of the cosmic baryons at  $z = 0$  are in the form of a diffuse intergalactic medium with temperature of  $10^5 \text{ K} < T < 10^7 \text{ K}$ , which has been called a warm-hot intergalactic medium (WHIM). Subsequent numerical simulations (e.g., Davé et al. 2001) and more recent observational data interpretation (Ferrara et al. 2005) also generally support this picture. However, a significant part of the baryons is still unaccounted for (Danforth & Shull 2008). Thus, the question of missing baryons/metals physical condition is still open (Bregman et al. 2009). Many current and future UV/X-ray missions (HST<sup>1</sup>, Chandra<sup>2</sup>, XMM-Newton<sup>3</sup>, GALEX<sup>4</sup>, FUSE<sup>5</sup>, World Space Observatory – WSO: SPECTRUM-UV<sup>6</sup>, SPECTRUM-X-GAMMA<sup>7</sup>, as well as XEUS<sup>8</sup>) aim to find solution of it. In many numerical efforts for solving this question the equilibrium cooling rates (e.g., Cen & Fang 2006; Yoshikawa & Sasaki 2006; Crain et al. 2009) are used. Obviously, feedback from galactic winds, supernova explosions and ionizing radiation from galaxies and quasars move the WHIM away from the equilibrium. In this context nonequilibrium cooling rates and ionization states are a necessary component of the WHIM ionic composition study.

The paper is organized as follows. In Section 2 we describe the details of the model and tests. In Section 3 we present our results and discuss possible applications. In Section 4 we summarize our results.

## 2 ATOMIC DATA AND MODEL DESCRIPTION

We study the ionization and thermal evolution of a Lagrangian element of cooling gas. A gas parcel is assumed to be optically thin for external ionizing radiation. In our calculations we consider all ionization states of the elements H, He, C, N, O, Ne, Mg, Si and Fe. We take into account the following major processes: photoionization, multi-electron Auger ionization process, collisional ionization, radiative and dielectronic recombination as well as charge transfer in collisions with hydrogen and helium atoms and ions. If we define the fraction of the ion stage  $i$  as  $X_i$ , then the time-dependent evolution of  $X_i$  is determined by

$$\begin{aligned} \frac{dX_i}{dt} = & -\gamma_i X_i - \alpha_i X_i n_e - \beta_i X_i n_e \\ & -(\zeta_i^{\text{H}} n_{\text{HI}} + \zeta_i^{\text{He}} n_{\text{HeI}} + \eta_i^{\text{H}} n_{\text{HII}} + \eta_i^{\text{He}} n_{\text{HeII}}) X_i \\ & + \alpha_{i+1} X_{i+1} n_e + \beta_{i-1} X_{i-1} n_e \\ & + (\zeta_{i-1}^{\text{H}} n_{\text{HI}} + \zeta_{i-1}^{\text{He}} n_{\text{HeI}}) X_{i-1} \\ & + (\eta_{i+1}^{\text{H}} n_{\text{HII}} + \eta_{i+1}^{\text{He}} n_{\text{HeII}}) X_{i+1} \end{aligned} \quad (1)$$

<sup>1</sup> <http://www.stsci.edu/hst/>

<sup>2</sup> <http://chandra.harvard.edu/>

<sup>3</sup> <http://xmm.vilspa.esa.es/>

<sup>4</sup> <http://www.galex.caltech.edu/>

<sup>5</sup> <http://fuse.pha.jhu.edu/>

<sup>6</sup> <http://wso.inasan.ru/>

<sup>7</sup> [http://hea.iki.rssi.ru/SXG/YAMAL/project\\_eng.htm](http://hea.iki.rssi.ru/SXG/YAMAL/project_eng.htm)

<sup>8</sup> <http://www.esa.int/science/xeus>

$$+\sum_{j<i}\gamma_{j\rightarrow i}x_j,$$

here  $\gamma$  is the photoionization rate of each ion, given by

$$\gamma_i = 4\pi \int_{\nu_{i,0}}^{\infty} \frac{J_\nu}{h\nu} \sigma_{i,\nu} d\nu, \quad (2)$$

and  $\nu_{i,0}$  is the ionization frequency,  $J_\nu$  is the background radiation flux,  $n_{\text{HI}}, n_{\text{HII}}, n_{\text{HeI}}, n_{\text{HeII}}$  and  $n_e$  are the number densities for neutral hydrogen, ionized hydrogen, neutral helium, ionized helium, and electrons, respectively,  $\sigma_{i,\nu}$  is the photoionization cross section adopted from Verner et al. (1996), Verner & Yakovlev (1995),  $\alpha$  is the recombination rate, including radiative recombination (Shull & van Steenberg 1982; Arnaud & Rothenflug 1992; Verner et al. 1996; Badnell 2006a), and dielectronic recombination (Badnell 2006b; Bautista & Badnell 2007; Colgan et al. 2003, 2004; Altun et al. 2004, 2006; Zatsarinny et al. 2003, 2004a,b, 2006; Mitnik & Badnell 2004; Mazzotta et al. 1998; Badnell 2006c), and  $\beta$  is the collisional ionization rate adopted from Voronov (1997),  $\eta^{\text{H}}, \eta^{\text{He}}, \zeta^{\text{H}}, \zeta^{\text{He}}$  are the charge transfer rates of ionization and recombination with hydrogen and helium adopted from Arnaud & Rothenflug (1985) and Kingdon & Ferland (1996),  $\gamma_{j\rightarrow i}$  is the total photoionization rate including that from deep shells followed by Auger-electron ejection, the Auger effect probabilities are taken from Kaastra & Mewe (1993).

The system (1) must be complemented by the temperature equation. Neglecting the change of number of particles in the system (for fully ionized hydrogen and helium it remains approximately constant) the gas temperature is determined by

$$\frac{dT}{dt} = \frac{n\Gamma - n_e n_H \Lambda}{Ank_B} \quad (3)$$

where  $n$ ,  $n_e$  and  $n_H$  are the electron and total hydrogen number densities,  $\Gamma(x_i, T, Z, J_\nu)$ ,  $\Lambda(x_i, T, Z)$  are heating and cooling rates,  $A$  is a constant equal to  $3/2$  for isochoric and  $5/2$  for isobaric cooling,  $k_B$  is the Boltzman constant. Cooling is isobaric when the cooling time is much greater than the dynamical time of a system,  $t_c/t_d \gg 1$  and it is isochoric when the time ratio is opposite,  $t_c/t_d \ll 1$ . In the lack of a dynamic determination we are able to constrain the dynamical time only by the age of the universe,  $t_H \sim 2/3H(t)$ . Hot gas ( $T > 10^6$  K) with low overdensities,  $\delta = (\rho - \langle \rho_b(z) \rangle) / \langle \rho_b(z) \rangle \sim 1$ , has cooling time higher than the local Hubble time. In this case the adiabatic approximation is a good choice.

The total cooling and heating rates are calculated using the photoionization code CLOUDY (ver. 08.00, Ferland et al. 1998). More specifically, we input into CLOUDY code a given set of all ionic fractions  $X_i$  calculated at temperature  $T$ , gas number density  $n$  and external ionization flux  $J(\nu)$  and obtain the corresponding cooling and heating rates. For the solar metallicity we adopt the abundances reported by Asplund et al. (2005), except Ne for which the enhanced abundance is adopted (Drake & Testa 2005). The solar abundances are listed in Table 1. In all our calculations we assume the helium mass fraction  $Y_{\text{He}} = 0.24$ .

We are interested in the ionization and thermal evolution of gas exposed to external ionizing radiation. A shape of ionizing background spectrum gives information about population of sources which give major contribution to the

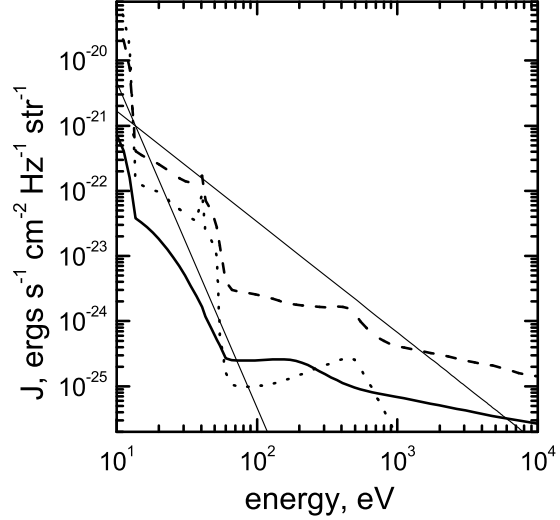


**Figure 1.** The ionizing backgrounds. The Haardt & Madau (2001) spectra at redshifts  $z = 0, 3, 6$  are depicted by thick solid, dashed and dotted lines correspondingly. The power-law profiles with  $J_{21} = 1$  and the spectral index  $\alpha = 1.7, 5$  are presented by thin solid lines.

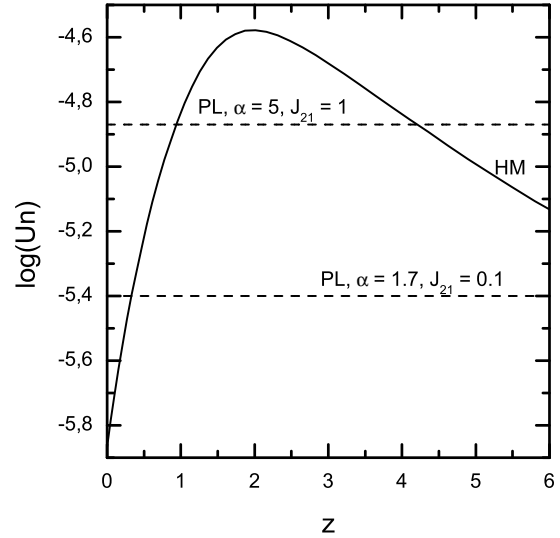


**Figure 2.** The parameter  $Un$  ( $U$  is the ionization parameter) for the Haardt & Madau (2001) spectra (HM) – solid line, and the power-law spectra (PL) – dash lines.

background. An exposed gas can be either located both near galaxy or quasar, or far from any source. In the former the ionizing radiation is inherent to a particular source, in the latter the gas is radiated by the extragalactic background formed by the galactic and quasar population.

Here we consider two types of spectra: a power-law spectrum, which is typical to stellar populations of galaxies, active galactic nuclei and quasars, and the extragalactic background calculated by using the radiative transfer in the cosmological simulations (Haardt & Madau 1996,

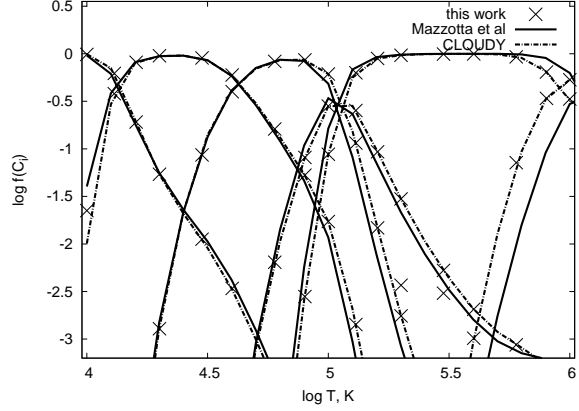
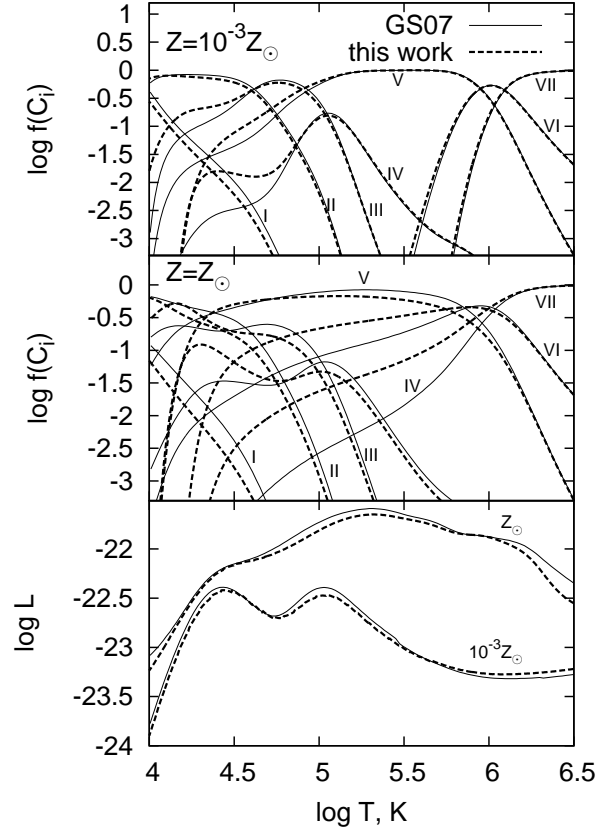
**Table 1.** Solar elemental abundances

Element	(X/H) <sub>⊙</sub>
Carbon	$2.45 \times 10^{-4}$
Nitrogen	$6.03 \times 10^{-5}$
Oxygen	$4.57 \times 10^{-4}$
Neon	$1.95 \times 10^{-4}$
Magnesium	$3.39 \times 10^{-5}$
Silicon	$3.24 \times 10^{-5}$
Iron	$2.82 \times 10^{-5}$

2001, HM01). A power-law (PL) spectrum shape is  $J = J_{21}(\nu/\nu_H)^{-\alpha}$ , where  $J_{21}$  is the flux value at the hydrogen ionization limit in units  $10^{-21} \text{ erg s}^{-1} \text{ cm}^{-2} \text{ str}^{-1}$ ,  $\alpha$  is the spectral index. To study the photoionization of gas around a quasar  $\alpha$  is taken equal to 1.7, (Sazonov et al. 2004), but we note that other studies have found both softer and harder spectra, with a significant variance about this value (Zheng et al. 1997; Telfer et al. 2002; Scott et al. 2004). We note that the quasar spectra show a gradual flattening in the 0.2–2 keV band (e.g. Sazonov et al. 2004). Such a property can be clearly seen for the cumulative extragalactic background for  $E \gtrsim 1 \text{ keV}$  at redshifts 0 and 3, where the contribution from quasars is dominant. We have also made calculations for shallower spectrum,  $\alpha = 1$ , because some authors use this value (see e.g. Kitayama et al. 2001). To mimic the stellar cluster ionization background, we adopt the spectrum with  $\alpha = 5$ . For such a spectrum shape, the photon-number weighted average intensity above 13.6 eV is close to that for the blackbody spectrum with an effective temperature  $\sim 2 \times 10^4 \text{ K}$  (Kitayama et al. 2001). Certainly, to model an adequate stellar cluster spectrum the theoretical starburst calculations are necessary. However, such models depend on many parameters, e.g., initial mass function, star formation efficiency, etc. Therefore, we have adopted a simple power-law shape. To model the influence from the extragalactic ionizing background we use the Haardt & Madau (2001) ionizing radiation flux, which is included in CLOUDY code. In our simulations we take the radiation spectrum from 1 to  $10^4 \text{ eV}$ . Figure 1 presents the ionizing background profiles used in our calculations. It is worth noting that the original spectra presented by HM01 do not include the absorption in the He II resonant lines (Madau & Haardt 2009; Faucher-Giguère et al. 2009), although such an absorption can change the abundances of metal ions like CIII and SiIV (Madau & Haardt 2009) at redshifts before the helium reionization.

To characterize an ionizing background it is convenient to use the ionization parameter  $U$  defined as the dimensionless ratio of hydrogen ionizing photons to the total hydrogen density. For a power-law spectrum with the spectral index  $\alpha$ , the ionization parameter can be easily found:  $U = 6.8 \times 10^{-5} J_{21}/n\alpha$ . Figure 2 shows the parameter  $Un$ , where  $n$  is the total number density, for the extragalactic ionizing background (HM01).

We solve a set of 96 coupled equations (95 for ionization states and one for temperature) using a Variable-coefficient Ordinary Differential Equation solver (Brown et al. 1989). The time step is chosen equal to the minimum value between

**Figure 3.** The collisional equilibrium carbon state fractions for our code (crosses) are superposed on the results by Mazzotta et al. (1998) (solid lines) and the standard collisional equilibrium test of CLOUDY (dash-dotted lines).**Figure 4.** The collisional time-dependent carbon state fractions for our code (thick dashed lines) are superposed on the results by Gnat & Sternberg (2007) shown by thin solid lines for metallicities  $10^{-3} Z_{\odot}$  (upper panel) and solar value (middle panel). The roman numbers indicate the ionization state. The collisional time-dependent cooling rates obtained from our code (thick dashed lines) and Gnat & Sternberg (2007) data (thin solid lines) for  $10^{-3} Z_{\odot}$  (lower curves) and solar (upper curves) metallicities are shown in the lower panel.



$(0.1t_{ion}, 0.01t_{cool})$ , where  $t_{ion}$  and  $t_{cool}$  are the ionization and cooling times, correspondingly.

The evolution of gas certainly depends on a choice of the initial condition of gas, namely, the initial ionic composition and temperature. We consider such a dependence elsewhere (some analysis can be found in Vasiliev et al. 2010). In this paper we start our calculations from temperature  $T = 10^8$  K with the collisional equilibrium ion abundances. At the beginning we present several tests of the method of calculation. In these tests we also start our calculations from temperature  $T = 10^8$  K with the collisional equilibrium ion abundances. During the calculation the gas number density is assumed to remain unchanged due to any dynamical or chemical processes. We stop our calculations when the temperature reaches  $10^4$  K or photoionization heating rate differs from cooling rate by less than 5% ( $|\Gamma - \Lambda|/\Lambda < 0.05$ ). The ionic composition is almost "frozen" at this moment. Note that with such a stopping criterion a gas still remains "time-dependent" at the end of the calculation, as it has not yet reached ionization equilibrium.

Figures 3-4 present the main tests of our code used for the calculations. At first we tested our model by comparing calculations in the collisional equilibrium (we run the simulations long enough at constant temperature so that eventually all ion species settle in ionization equilibrium). Figure 3 shows the carbon ionization fractions in the collisional equilibrium obtained from our code (depicted by crosses) and the results by Mazzotta et al. (1998) as well as the standard CIE test of the CLOUDY code. One can see a good coincidence between the results of our code and those obtained in the previous works.

Two upper panels of Figure 4 presents the carbon ionization fractions in the collisional time-dependent case obtained from our code and the results by Gnat & Sternberg (2007). One can see that the fractions in both calculations are close to each other for low metallicity value,  $Z = 10^{-3} Z_{\odot}$ , while the strong deviations can be found for solar metallicity. We expect that this difference is due to various atomic data and, as a consequence, ionization and thermal evolution. Actually, Gnat & Sternberg (2007) have utilized the CLOUDY code ver.06.00, whereas in our calculations more recent version (08.00) of the code is used. There were several revisions of atomic data between these versions<sup>9</sup>. Also we don't include in our code the cooling rate by sulfur, but small variation in the total cooling rate can produce different ionic composition. Thus, in low metallicity gas the ionic composition obtained in our code is close to that of Gnat & Sternberg (2007), because the thermal evolution is determined by hydrogen and helium. Whereas the increase of metallicity leads to stronger deviation between our and Gnat & Sternberg (2007) results. Note that the total cooling rates in both calculations are close, the rates are shown in the lower panel of Figure 4.

### 3 RESULTS

In this section we consider the isochoric cooling rates and the ionization states. We leave out of scope of this paper the iso-

baric cooling, because the increase of gas density during isobaric process, obviously, leads to the collisionally controlled ionization states and radiative cooling (the increase factor of density is  $10^4$  if we study the gas evolution from  $10^8$  to  $10^4$  K).

#### 3.1 Cooling rates

In Table 2 we list the main parameters of the models considered here<sup>10</sup>. We start from temperature  $T_i = 10^8$  K with the collisional equilibrium ion abundances. This seems to be a good approximation, because the ionic composition at so high temperature is mainly determined by frequent collisions.

##### 3.1.1 Dependence on metallicity for power-law spectrum

Figure 5 shows the cooling rates for gas exposed to external radiation for several models listed in Table 2. In the panel (a) the dependence of cooling efficiency on the gas metallicity is presented. The other parameters are fixed:  $n = 10^{-4} \text{ cm}^{-3}$ ,  $J_{21} = 1$  and  $\alpha = 1.7$ . In addition, the collisional nonequilibrium cooling rates for the same metallicities are depicted by thin lines. A substantial difference between the cooling rates of photoionized and collisional gas at temperature lower  $10^6$  K is clearly seen. The cooling of photoionized gas is suppressed in contrast to that of collisionally ionized gas, because the gas is overionized due to photoionization. Indeed, one can see that the cooling rates of photoionized gas at  $T \sim 10^5$  K are smaller by an order of magnitude in comparison with that of collisionally ionized gas. An increase of metallicity provides more effective cooling of gas and shifts the maximum in the cooling rate to higher temperatures. In general, for the same physical state of gas the photoionization cooling rates are lower than the collisional ones.

##### 3.1.2 Dependence on flux amplitude and spectral index

In the panel (b) one can see the cooling rates for gas exposed to radiation with fluxes  $J_{21} = 0.01, 0.1, 1$ , the other parameters,  $\alpha = 1.7$ ,  $n = 10^{-4} \text{ cm}^{-3}$ ,  $Z = Z_{\odot}$ , were fixed. The cooling rate is getting suppressed significantly with increase of the flux. The panel (c) presents the cooling rates for three different values of the spectral index  $\alpha = 5, 1.7$  and  $1$ . In this case the picture is similar to the previous one. For less steep spectrum the cooling rate is suppressed stronger.

##### 3.1.3 Dependence on redshift for the extragalactic spectrum

The spectrum formed by a cumulative extragalactic radiation field from galaxies and quasars differs significantly from a simple power-law spectrum (see Figure 1). Consequently, the cooling rate of gas exposed to the extragalactic radiation also differs from that exposed to a power-law spectrum. Figure 5d presents cooling rates for gas with  $n = 10^{-4} \text{ cm}^{-3}$  and

<sup>9</sup> <http://wiki.nublado.org/wiki/RevisionHistory>

<sup>10</sup> The cooling rates and ionic composition for several models are available at <http://ism.rsu.ru/cool/cool.html>.

**Table 2.** List of models

$n, \text{cm}^{-3}$	$Z/Z_{\odot}$	spectrum
$10^{-4}, 10^{-3}, 10^{-2}$	$10^{-3} - 1$	power-law (PL), $\alpha = 1, 1.7, 5$ ; $J = (10^{-4}-1)J_{21}$
$10^{-4}, 10^{-3}, 10^{-2}$	$10^{-3} - 1$	Haardt & Madau (2001) data (HM), $z = 0 - 6$

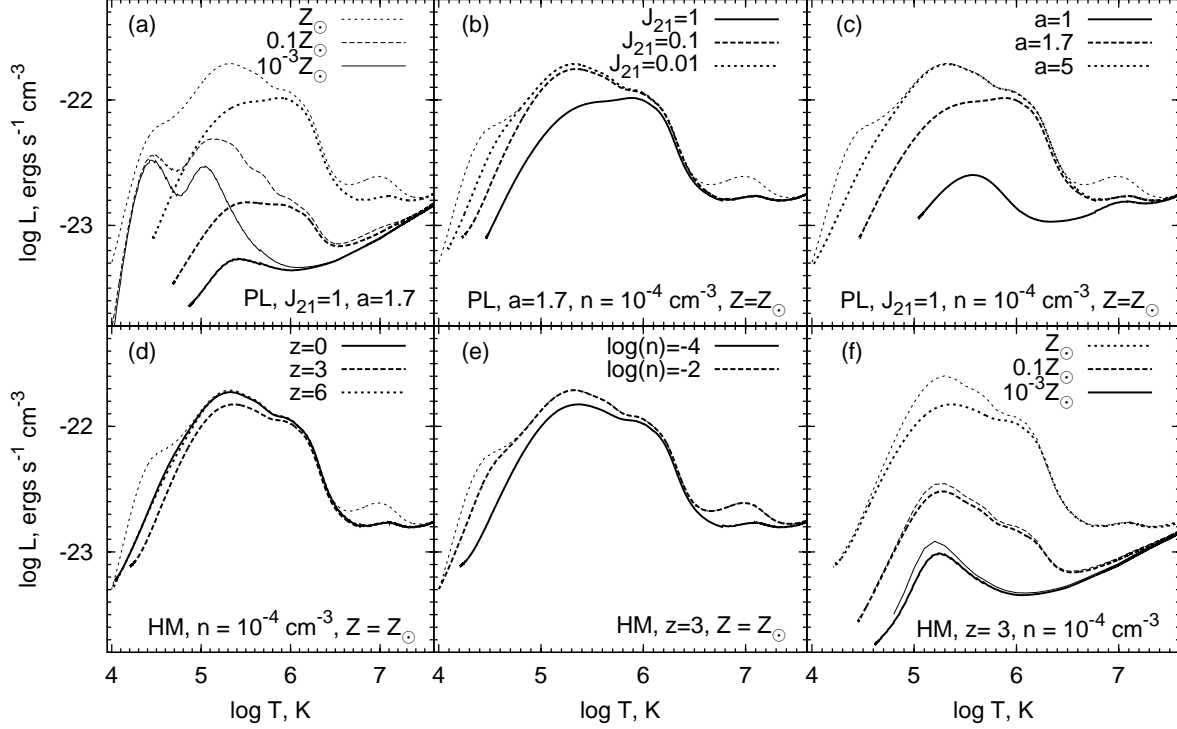


**Figure 5.** The cooling rates for gas exposed to ionizing radiation: (a) the dependence on metallicity for gas density  $n = 10^{-4} \text{ cm}^{-3}$  of gas exposed to the power-law (PL) external radiation with  $J_{21} = 1$  and  $\alpha = 1.7$ , the cooling rates for metallicity  $Z = 10^{-3}, 10^{-1}$  and  $1 Z_{\odot}$  are shown by thick solid, dashed and dotted lines, correspondingly, the cooling rates for pure collisional case are depicted by thin lines of the same type, (b) the dependence on flux amplitude  $J_{21}$  for power-law spectrum with  $\alpha = 1.7$  and gas with  $n = 10^{-4} \text{ cm}^{-3}, Z = Z_{\odot}$ , the cooling rates for  $J_{21} = 0.01, 0.1, 1$  are shown by thick dotted, dashed and solid lines, correspondingly; (c) the dependence on spectral index  $\alpha$  for gas with  $n = 10^{-4} \text{ cm}^{-3}, Z = Z_{\odot}$  exposed to  $J_{21} = 1$ , the cooling rate for  $\alpha = 1$  is shown by thick solid line, the rate for  $\alpha = 1.7$  – thick dashed line, and the rate for  $\alpha = 5$  – thick dotted line; (d) the rates for gas with  $n = 10^{-4} \text{ cm}^{-3}$  and solar metallicity exposed to the Haardt & Madau (2001) background radiation (HM), the solid, dashed and dotted lines correspond to the backgrounds at redshifts  $z = 0, 3, 6$ ; (e) the rates for gas with solar metallicity and number densities  $n = 10^{-4}, 10^{-2} \text{ cm}^{-3}$  (thick solid and dashed lines, correspondingly) exposed to the Haardt & Madau (2001) background radiation at  $z = 3$ ; (f) the nonequilibrium (thick) and photoequilibrium (thin lines) cooling rates for gas with  $n = 10^{-4} \text{ cm}^{-3}$  and metallicities  $Z = 10^{-3}, 10^{-1}, 1 Z_{\odot}$  (solid, dash and dot lines, correspondingly) exposed to the Haardt & Madau (2001) background radiation at  $z = 3$ , the photoequilibrium rates are similar to those obtained by Wiersma et al. (2009), see details in the text; In all panels, except (a) and (f), the collisionally induced cooling rate for gas with  $n = 10^{-4} \text{ cm}^{-3}, Z = Z_{\odot}$  is depicted by thin dotted line.

solar metallicity exposed to the HM01 extragalactic background spectra at redshifts  $z = 0, 3, 6$ . Among these redshifts the ionizing radiation flux is the strongest at  $z = 3$ , so a difference from the collisional cooling rate is the most significant at  $z = 3$ . The cooling rates for two other redshifts presented here coincide between each other. In comparison with the collisional case the rates demonstrate notable differences at  $T < 10^6 \text{ K}$  for  $z = 3$  and  $T \lesssim 8 \times 10^4 \text{ K}$  for  $z = 0$  and  $6$ . Such differences are caused by the overionization of the dominant coolants. A more detailed discussion can be found in the next subsection.

### 3.1.4 Dependence on density and metallicity for the extragalactic spectrum at $z = 3$

Figure 5e shows the dependence of the cooling rates on gas density. This dependence is determined by the collisional ionization and photoionization time ratio, which is proportional to  $n_e/J_{21}$ . A higher ionizing flux leads to a predominance of the photoionization, whereas an increase of density intensifies the collisional ionization. For instance, the cooling rates of collisional and photoionized gas with  $n = 10^{-2} \text{ cm}^{-3}$  (panel e) are equal to each other at  $T \gtrsim 5 \times 10^4 \text{ K}$ . A small difference at lower temperature is determined by the overionization of hydrogen, carbon and

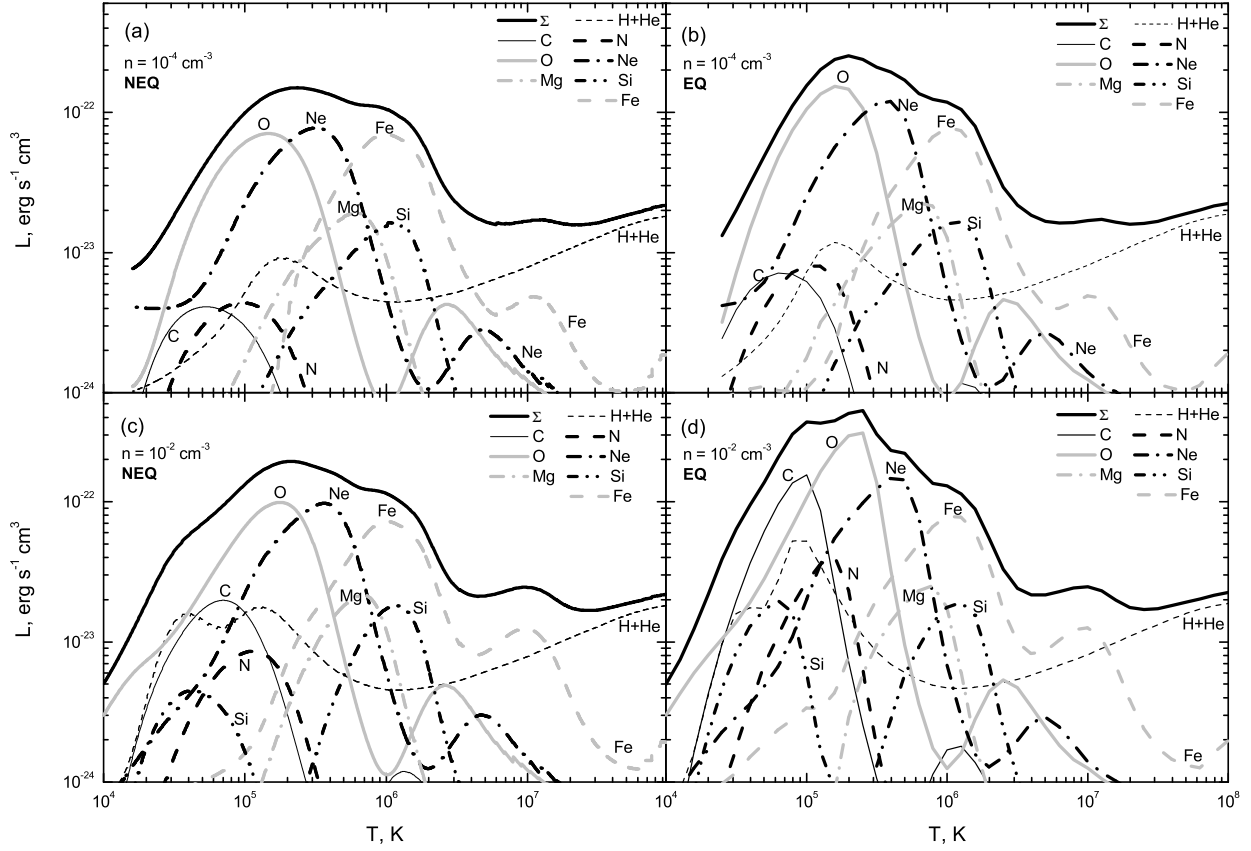


**Figure 6.** The cooling rates in photo-nonequilibrium (left panels) and photo-equilibrium (right panels) for gas with solar metallicity and  $n = 10^{-4} \text{ cm}^{-3}$  (upper panels) and  $n = 10^{-2} \text{ cm}^{-3}$  (lower panels), exposed to the extragalactic HM ionizing radiation at redshift  $z = 3$ . The thick solid black line shows the total cooling rate, the thin dash line shows the contribution from hydrogen and helium, the other lines (see the legend on the panels) show the contributions from each chemical element.

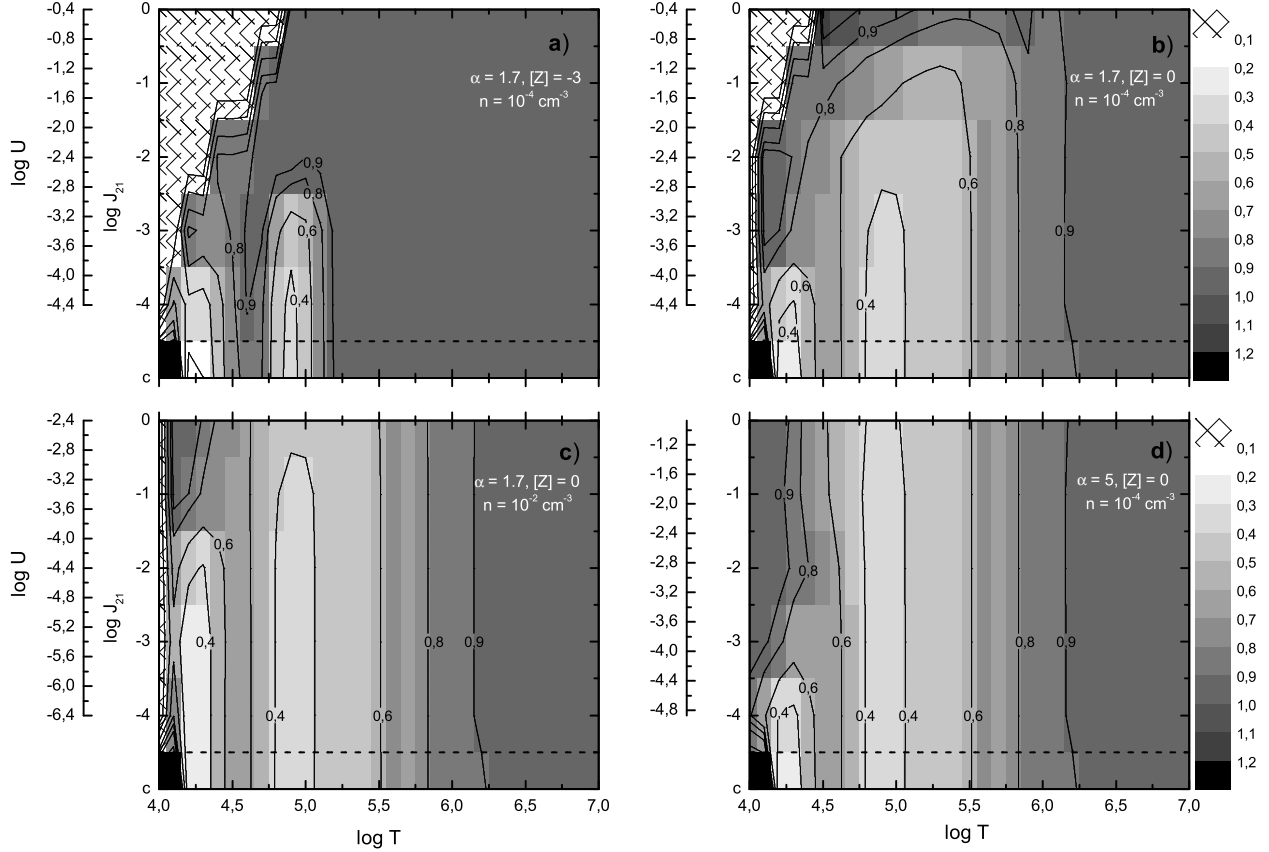
oxygen, which are the main contributors to the cooling rate in this temperature range.

Figure 5f shows the dependence on metallicity of nonequilibrium cooling rates for gas with number density  $n = 10^{-4} \text{ cm}^{-3}$  exposed to the HM01 spectrum at  $z = 3$ . They differ considerably from the nonequilibrium collisional rates presented on the panel (a). The presence of UV radiation leads to overionized ionic composition, consequently, suppresses the cooling rates.

Recently Wiersma et al. (2009) have calculated the cooling rates in the photoionization equilibrium. Because of the restricted number of the chemical elements and its different abundances in our model we recalculate photoequilibrium rates similar to Wiersma et al. (2009) and compare it to the nonequilibrium photoionization cooling rates. We add the corresponding cooling rates in Figure 5f. One can see a good coincidence between the equilibrium and the nonequilibrium cooling rates of photoionized gas for  $Z \leq 0.1 Z_{\odot}$ . This coincidence is a result of the influence of the ionizing radiation, whereas for the collisional case the equilibrium and the nonequilibrium cooling rates differ significantly (e.g., Sutherland & Dopita 1993). A sufficiently high ioniz-

ing radiation flux forces the ionic composition to settle onto the equilibrium, though a small difference is seen for solar metallicity at  $T \sim 2 \times 10^5 \text{ K}$ . Therefore, one can expect that nonequilibrium effects will become more significant for higher metallicity.

Let us consider the difference between the nonequilibrium (time-dependent) and photoequilibrium cooling rates. Figure 6 shows the individual contributions from each chemical element to the total cooling rate for gas exposed to the HM01 extragalactic ionizing radiation at  $z = 3$  in the photo-nonequilibrium (left panels) and photoequilibrium (right panels). Figure 6 presents the rates for solar metallicity and two number densities,  $10^{-4}$  and  $10^{-2} \text{ cm}^{-3}$ . The time-dependent rates coincide with the photoequilibrium ones at  $T \gtrsim 10^6 \text{ K}$ . At the same time, for  $T \lesssim 10^6 \text{ K}$  the total cooling rates for both densities differ significantly in the photoequilibrium and time-dependent models. This difference comes from individual contributions of the considered elements. One can see that the contributions from C, N, O and Ne in the time-dependent case are smaller than those in the equilibrium. These elements are overionized in the time-dependent case. Such a picture is determined by the



**Figure 7.** The ratio of nonequilibrium to equilibrium cooling rates for gas exposed to a power-law spectrum: a)  $n = 10^{-4} \text{ cm}^{-3}$ ,  $Z = 10^{-3} Z_{\odot}$  and the index  $\alpha = 1.7$ ; b)  $n = 10^{-4} \text{ cm}^{-3}$ ,  $Z = Z_{\odot}$  and  $\alpha = 1.7$ ; c)  $n = 10^{-2} \text{ cm}^{-3}$ ,  $Z = Z_{\odot}$  and  $\alpha = 1.7$ ; d)  $n = 10^{-4} \text{ cm}^{-3}$ ,  $Z = Z_{\odot}$  and  $\alpha = 5$ . The ionization parameter  $U$  corresponded to the spectrum and number density is shown by extra y-axis. The letter "c" on the y-axis (or the area is separated by dash line) corresponds to the ratio of the cooling rates of collisional plasma (no photoionization). The shaded area corresponds to the conditions under which the photoheating exceeds the cooling in the nonequilibrium case.

recombination timescales of the C, N, O and Ne ionic states, which lead to the recombination lag in the time-dependent model. For  $n = 10^{-2} \text{ cm}^{-3}$  the hydrogen and helium should be added to the list of the overionized ions. Panels (c-d) show a strong difference in the H&He contributions. For  $n = 10^{-2} \text{ cm}^{-3}$  collisions dominate over photoionization in a wide temperature range, so the photo-nonequilibrium cooling rate coincides with the collisional one at  $T \gtrsim 5 \times 10^4 \text{ K}$  (see Figure 5e) and the photoequilibrium and CIE cooling rates equal to each other at  $T \gtrsim 4 \times 10^4 \text{ K}$ . Below  $T \sim 4 \times 10^4 \text{ K}$  the difference between photoequilibrium and CIE cooling rates is mainly determined by the overionization of hydrogen and it is maximal at  $T \sim 2 \times 10^4 \text{ K}$  (the ratio of the rates in photoequilibrium to that in the CIE reaches a factor of 5). In general, further increase in the number density leads to the domination of collisions in wider temperature range. It is interesting that for  $n = 10^{-2} \text{ cm}^{-3}$  the contributions from carbon and nitrogen are higher than these for  $n = 10^{-4} \text{ cm}^{-3}$ , e.g. for carbon the increasing fac-

tor reaches about a factor of 5 around  $T \simeq 7 \times 10^5 \text{ K}$ , where it provides the maximum contribution.

### 3.1.5 Importance of nonequilibrium effects

In order to determine a parameter space, where nonequilibrium effects play a significant role we calculate two sets of models: one is for power-law spectra,  $\alpha = 1.7$  and 5, the other is for the HM01 extragalactic background.

Figure 7 presents the ratio of the nonequilibrium to equilibrium cooling rates for gas exposed to a power-law spectrum with  $\alpha = 1.7$  (panels (a-c)) and  $\alpha = 5$  (panel (d)). To compare easily the ratio of the cooling rates of collisional and photoionized plasma the ratio of collisional gas (no photoionization) is shown by the letter "c" on the y-axis (the area is separated by dash line) on each panel of Figure 7. In the panels (a) and (b) the ratio is shown for  $Z = 10^{-3} Z_{\odot}$  and the solar metallicities. As one expects the photoequilibrium and time-dependent cooling rates are almost equal for the lower metallicity. Only for both  $J_{21} \lesssim 10^{-3}$  and  $T \lesssim 10^5 \text{ K}$



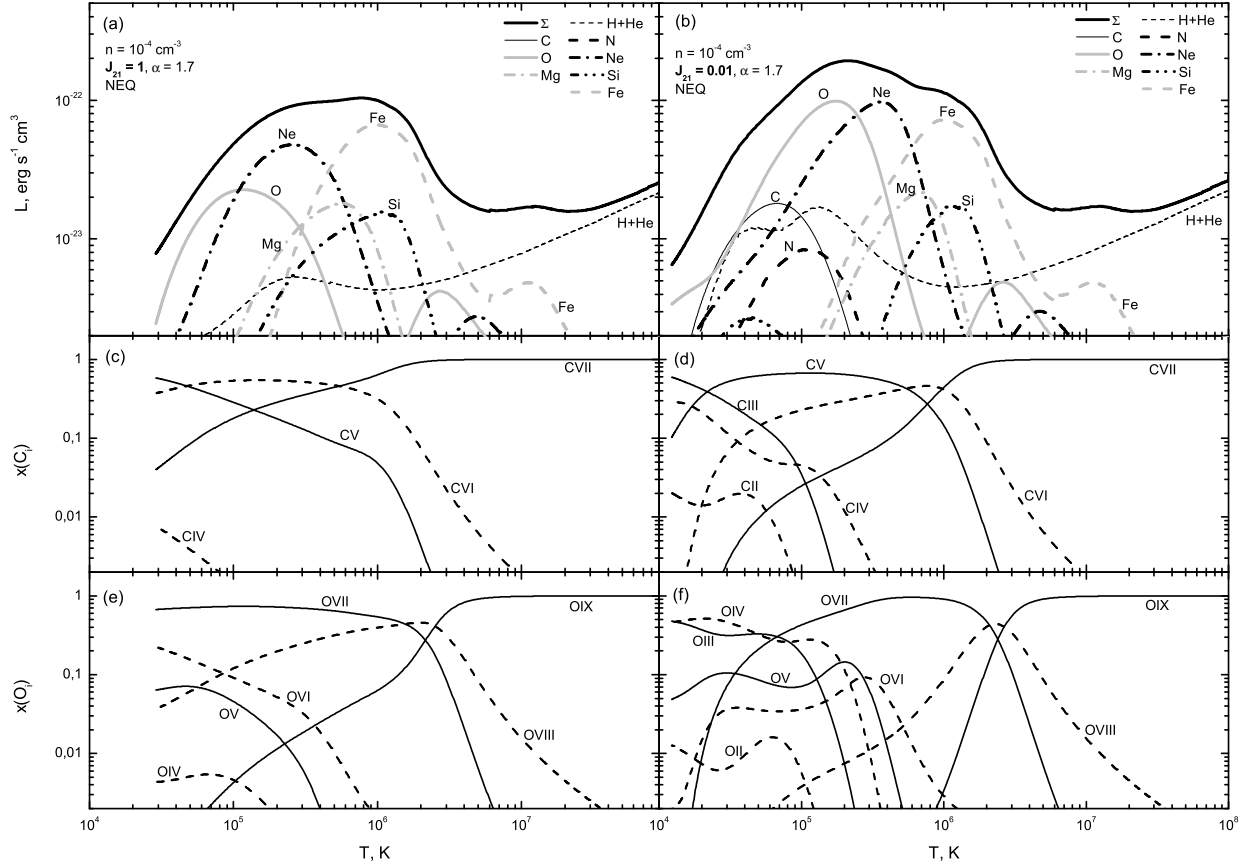


**Figure 8.** The cooling rates, carbon and oxygen ionization states in photo-nonequilibrium for solar metallicity and  $n = 10^{-4} \text{ cm}^{-3}$  exposed to the power-law ionizing radiation with  $J_{21} = 1$  (left panels) and  $J_{21} = 0.01$  (right panels), the spectral index  $\alpha$  equals 1.7. The thick solid black line shows the total cooling rate, the thin dash line shows the contribution from hydrogen and helium, the other lines (see the legend on panels) show the contributions from each chemical element.

the rates demonstrate a difference, which originates from the efficient H and He recombination in the photoequilibrium for such a low ionizing flux. For solar metallicity (panel b) the deviation between the rates can be found in wider range of both flux and temperature. The time-dependent rates tend to the photoequilibrium at  $J_{21} \gtrsim 1$  (e.g. the ratio is close to 1) that corresponds to the ionization parameter  $\log U \gtrsim -0.4$  (see the extra  $y$ -axis). The increase of density,  $n = 10^{-2} \text{ cm}^{-3}$ , leads to further expansion of the range (panel c), where the photoequilibrium and photo-time-dependent rates show a significant difference. Under such conditions the photo-nonequilibrium rate tends to that in the collisionally cooling gas (the region below the dashed line). So the maximum difference between photoequilibrium and photo-nonequilibrium rates corresponds to that between the CIE and collisionally time-dependent cooling rates (note that a significant difference between the collisional equilibrium and nonequilibrium rates at  $T \lesssim 2 \times 10^4 \text{ K}$  is determined by the efficient hydrogen recombination in the CIE). Similar difference can be seen in the panel (d), where the ratio is presented for the steeper spectrum,  $\alpha = 5$ . Note that

in the panels (b) and (d) the ratios are presented for the different power-law index  $\alpha$ , so the difference between the ratios at a given  $U$  for the power-law spectra with  $\alpha = 1.7$  and 5 is due to the different photon distribution (in general, the dependence of cooling rates on ionization parameter can be considered if the same photon distribution is used). This difference is clearly seen for  $\log U = -1.4$  and can be explained by stronger overionization of high ionic states by hard (far UV and X-ray) photons and longer recombination lag for the spectrum with  $\alpha = 1.7$  in comparison with that for the steeper spectrum with  $\alpha = 5$ . The number of such hard photons is larger for  $\alpha = 1.7$  than for  $\alpha = 5$ , although the number of the hydrogen ionizing photons is the same for both spectra.

Panels (a-b) in Figure 8 present the individual contributions from each chemical element into the total cooling rate for gas with solar metallicity exposed to the power-law ionizing radiation with  $J_{21} = 1$  (a) and  $J_{21} = 0.01$  (b), the spectral index  $\alpha$  equals 1.7. At  $T \gtrsim 2 \times 10^6 \text{ K}$  the total cooling rates are very close to each other as well as almost equal to the photoequilibrium cooling rates (see Fig-

ure 7b). In this temperature range the H, He and Fe ions provide the main contribution to the rate. At such a high temperature contribution of H and He is due to thermal bremsstrahlung. Below this temperature the cooling by the Fe, Ne, O and C ions dominate. The contributions from Fe and Ne are significant in the ranges  $T \lesssim (0.6 - 2) \times 10^6$  and  $T \lesssim (1 - 6) \times 10^5$ , correspondingly, for both fluxes considered here. If the flux (the ionization parameter  $U$ , in general) increases, then the Ne cooling bump strongly diminishes. This trend can be clearly seen in the panels (a) and (b). Further increase of the ionizing flux leads to the Fe bump diminishing. In Figure 8 similar situation can be seen for the O and especially for C cooling bumps at  $T \sim 10^5$  K. Actually, for  $J_{21} = 1$  the contribution from oxygen dominates only at  $T$  below  $10^5$  K, but for  $J_{21} = 0.01$  oxygen becomes a major coolant at  $T \lesssim 2 \times 10^5$ . Carbon demonstrates more remarkable increase of the cooling rate: for  $J_{21} = 1$  its contribution is negligible, but for  $J_{21} = 0.01$  it gives a significant part of the cooling rate and even becomes one of the dominant coolant at  $T \sim (2 - 4) \times 10^4$  K. We note that for  $J_{21} = 1$  the difference of cooling rate between photoequilibrium and nonequilibrium is low as  $\sim 10\%$ , so the ionic composition is expected to be close to the photoequilibrium: the Ne and Fe ions are slightly overionized. The opposite situation is for  $J_{21} = 0.01$ , the difference of the cooling rates reaches a factor of two at  $T \simeq 2 \times 10^5$  K. Under such a flux the ions of the main coolants (C, O, Ne and Fe) are strongly overionized in the range  $T \lesssim 10^6$  K, where the difference of the cooling rates becomes significant (see Figure 7b). The Mg and Si give a minor contribution in the whole temperature range for two fluxes considered.

Figure 8(c-f) present the carbon and oxygen ionization states in a gas exposed to the power-law ionizing radiation with  $J_{21} = 1$  (left panels) and  $J_{21} = 0.01$  (right panels) with the spectral index  $\alpha = 1.7$ . For  $J_{21} = 1$  the increase of the cooling by oxygen at  $T \lesssim 5 \times 10^5$  K is certainly determined by OVI and OV ions (see panel (e)). The contribution from oxygen at  $T \lesssim 5 \times 10^4$  K is probably to go down due to the existence of the high ionic states only, OV-OVII, whose cooling rate is inefficient in this temperature range. Carbon is strongly ionized and the CV-CVII ions do not provide any significant energy losses. For the lower flux,  $J_{21} = 0.01$ , the photoionization rate is smaller and the recombination becomes more efficient. The contribution from carbon at  $T \lesssim 2 \times 10^4$  K is determined by the rapid increase of the CIII and CIV ion abundances. The dominant contribution from oxygen in the wide temperature range can be explained by the OV-OVI ions at  $T \gtrsim 10^5$  K and the OIII-OIV ions at  $T \lesssim 10^5$  K. Note that for a photoionized gas the decrease of metallicity leads to increase of the H and He contribution to the cooling rate. The cooling of low metallicity gas,  $Z \sim 10^{-3} Z_{\odot}$ , controlled by H and He ions only, the contribution from other elements is negligible.

Figure 9 demonstrates the ratio for the HM01 background spectrum at redshift  $z$ . For the extragalactic HM01 background the picture is similar to that for a power-law spectrum: an increase of the metallicity leads to an increase of the magnitude of deviations from the equilibrium. For low metallicity,  $Z \sim 10^{-3} Z_{\odot}$ , the ratio remains close to unity in the wide range of temperature. Only for  $T \sim 10^5$  K it deviates from unity about 20-30% that is determined by the overionization of helium (see Figure 5f). Figure 9 shows

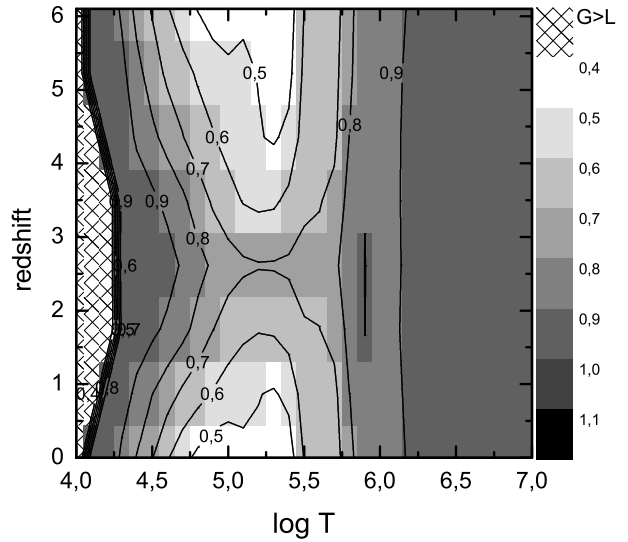


**Figure 9.** The ratio of nonequilibrium to equilibrium cooling rates for gas with density  $n = 10^{-4} \text{ cm}^{-3}$  and solar metallicity exposed to the Haardt & Madau (2001) background spectrum at redshift  $z$ . The shaded area corresponds to the conditions under which the photoheating exceeds the cooling in the nonequilibrium case.

the ratio for solar metallicity. As one expects the nonequilibrium effects are important for  $T \lesssim 10^6$  K in the whole redshift range,  $z = 0 - 6$ . The maximum deviation reaches a factor of  $\sim 2$  at  $T \sim 10^5$  K for  $z \lesssim 1$  and  $z \gtrsim 5$ . As the extragalactic background is maximal around redshifts  $z = 2 - 3$  a saddle point on the surface of the cooling rate ratio is observed: the deviation from the equilibrium is minimum in this redshift range. As we mentioned above the difference from photoequilibrium is determined by smaller contribution to the cooling from C, N, O and Ne ions, because they are overionized. The ionizing flux in  $z = 2 - 3$  is the highest, so the ionic composition is moved to photoequilibrium (see the previous section). For both  $z \sim 0$  and  $z \sim 6$  the ionizing flux decreases and the difference from photoequilibrium becomes more clear.

Let us summarize where the photoequilibrium calculation can be used and how the parameters (metallicity, temperature, density and UV intensity) should be changed so that the nonequilibrium effects become important. The calculations presented above show that the photoequilibrium is reached in high-temperature gas,  $T \gtrsim 3 \times 10^6$  K, for any metallicity or ionization parameter. Note that the photoequilibrium equals to the CIE for such a high temperature. Below  $T \sim 3 \times 10^6$  K the deviation from the photoequilibrium grows. For a metallicity as low as  $10^{-3} Z_{\odot}$  such a deviation is minimum. The increase of metallicity leads to the widening of the parameter space, where nonequilibrium effects are significant (Figures 7 and 9), that is clearly seen for solar metallicity. This can be easily explained by the overionization of metal ions and the increase of the contribution from metals to the cooling rate for higher metallicity. For collisionally ionized gas the deviation from the equilibrium at  $T \lesssim 10^6$  K is significant for any metallicity.

**Table 3.** The transition from photo-EQ to NEQ at  $T < 10^6$  K.

the conditions, where $\Lambda^{EQ} \simeq \Lambda^{NEQ}$ is expected	a variation of parameters leads to $\Lambda^{EQ} \neq \Lambda^{NEQ}$
high ionization parameter $U$ (high UV flux/low density), $U \gtrsim 10^{-2}$ for $Z \lesssim 10^{-2} Z_{\odot}$ , $U \gtrsim 1$ for $Z \sim Z_{\odot}$	<i>either</i> increase of $Z$ <i>or</i> decrease of $U$ parameter (decrease of flux/increase of density)

In a gas exposed to ionizing radiation the photoequilibrium is reached faster than higher ionization parameter. At low ionization parameter (low flux intensity/high density), the differences between equilibrium and nonequilibrium indeed become large, but these are just the differences in the collisional case. Thus, in Table 3 for  $T < 10^6$  K we provide the parameter range under which the cooling rates in the equilibrium (EQ) and nonequilibrium (NEQ) are close, and a change of parameters, which violates this equality. Here we should also pay attention on that the ionization parameter  $U$  does not fully describe the spectrum and in general the transition from photoequilibrium to nonequilibrium depends on the ionizing spectrum shape.

As a conclusion we note that the deviation of the cooling rates between photoequilibrium and nonequilibrium is determined by recombination lag in the latter case. The maximum difference is for collisionally controlled gas. Such condition in gas is reached for ionization parameter as low as  $\log U \lesssim -5$  (see Figures 7–9). The difference decreases with the ionization parameter growth. For sufficiently high ionization parameter the photoequilibrium can be reached. However, the transition region from photoequilibrium to nonequilibrium is quite wide. For ionization parameter as low as  $\log U \sim -5$  the nonequilibrium collisional cooling rates and ionic composition are a better choice. The photoequilibrium is reached for ionization parameter as high as  $\log U \gtrsim -2$  for  $Z \lesssim 10^{-2} Z_{\odot}$  and  $\log U \gtrsim 0$  for  $Z \sim Z_{\odot}$  (see Table 3). For supersolar metallicity the photoequilibrium is expected to reach for higher ionization parameter. So where the physical conditions are favour to collisional ionization (the collisions dominate or its contribution to the total ionization rate is significant), the nonequilibrium (photo)ionization calculations should be conducted.

### 3.2 Ionization states of metals and their ratios

#### 3.2.1 Collisions or photoionization: CIII and CIV ions

In the previous sections we have considered the time-dependent cooling functions of a photoionized gas, their deviations from the photoequilibrium rates and the contribution to the cooling rate from chemical elements. We have found that the transition region from photoequilibrium to nonequilibrium is quite wide. Obviously, the reason of such a transition is the recombination lags in the nonequilibrium model. Consequently, a significant difference of the ionic ratios is expected between the photoequilibrium and the nonequilibrium. Moreover, which of two processes, collisions or photoionization, is dominant can be also identified using ionic ratios. For gas with a given density and metallicity exposed to an ionizing radiation the transition between col-

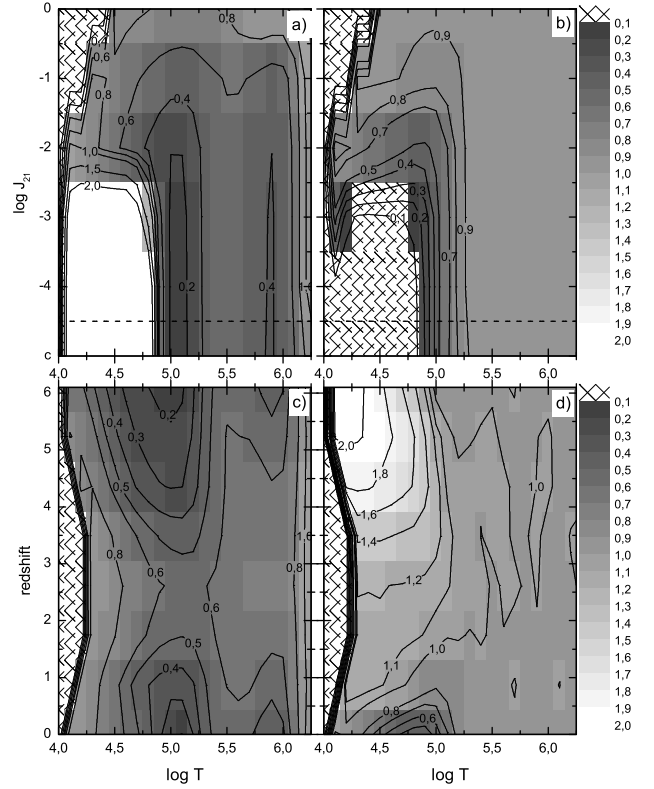


**Figure 10.** The ratio of the CIV ion fraction in the nonequilibrium case to that in the equilibrium (left panels), and the ratio,  $R = x(\text{CIII})/x(\text{CIV})$ , in the nonequilibrium to that in the equilibrium (right panels) for gas with density  $n = 10^{-4} \text{ cm}^{-3}$  and solar metallicity exposed to the power-law spectrum with  $\alpha = 1.7$  (upper row) and the Haardt & Madau (2001) background spectrum at redshift  $z$  (lower row). In the panels (a) and (c) The letter "c" on the y-axis (or the area is separated by dash line) corresponds to the ratio of the cooling rates of collisional plasma (no photoionization). The shaded area corresponds to the conditions under which the the ratio does not exist (photoheating exceeds the cooling in the nonequilibrium case) or the ratio is out of the ranges presented in the gray scale.

lisionally controlled or photoionization regimes depends on the photoionization rate, which is determined by spectrum shape and flux magnitude.

Figure 10 shows the ratio of the CIV ion fraction in nonequilibrium to that in photoequilibrium (left panels) for gas with density  $n = 10^{-4} \text{ cm}^{-3}$ , solar metallicity exposed to the power-law spectrum with  $\alpha = 1.7$  (upper) and the HM01 background spectrum at redshift  $z$  (lower). As one expects the CIV fraction in the photoequilibrium strongly differs from that in the time-dependent case: the ratio reaches several times. The significant deviation from photoequilibrium can be also found for the HM01 background. In the panel (a) one can see that the decrease of the UV flux amplitude leads to that the CIV fraction ratio tends to that in collisionally controlled gas. We should note once again that due to the recombination lag the carbon ionic states in the nonequilibrium are always overionized in comparison with these in the equilibrium (see the panels (a) and (c)):

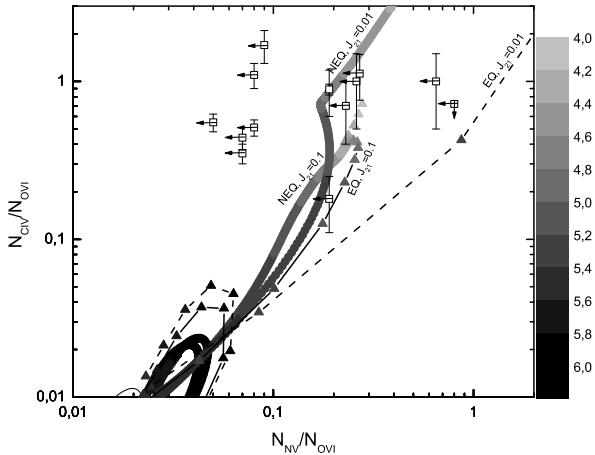


**Figure 11.** The dependence  $N_{\text{CIV}}/N_{\text{OVI}}$  versus  $N_{\text{NV}}/N_{\text{OVI}}$  in the photo-nonequilibrium model for cooling gas with  $n = 10^{-4} \text{ cm}^{-3}$  and  $Z = Z_{\odot}$  exposed to the ionizing radiation with  $\alpha = 1.7$  and two fluxes  $J_{21} = 0.01$  and  $0.1$  (the corresponding labels are shown). The same dependence in the photoequilibrium are by triangles connected by solid line for  $J_{21} = 0.1$  and by dashed line for  $J_{21} = 0.01$ . Gas temperature is indicated by gray scale along the trajectories: from hot (black) to cold (light gray) gas. The data points show the ionic ratios observed in metal absorbers (see Table 8 Fox et al. 2006).

where the ratio is below 1, the CV state dominates in the nonequilibrium, e.g. the CV is overionized, and in the opposite case, where the ratio is greater than 1, the CIV is overionized, whereas in the photoequilibrium under the same conditions the CIII fraction increases fastly. This is clearly seen in the right panels of Figure 10, where the ratio of the values,  $R = x(\text{CIII})/x(\text{CIV})$ , in the nonequilibrium to that in the equilibrium is presented. Indeed, in the panel (b) the shaded region in the bottom left corner corresponds to the ratio less than 0.1, i.e. the denominator of the ratio, the  $R$  value in the equilibrium, is high.

In the panel (d) the strong deviations of the  $R$  value from the photoequilibrium can be found for the HM01 spectrum. Because the CIII/CIV ratio is used as one of the important observable indicator to discriminate between the HeII reionization models (Schaye et al. 2003; Agafonova et al. 2007; Madau & Haardt 2009), we should pay attention on the significant difference at redshifts  $z = 2 - 3$ , when the HeII reionization is expected to occur. The nonequilibrium analysis of the CIII/CIV ratio in the absorption spectra obtained by (Agafonova et al. 2007) can be found in (Vasiliev et al. 2010). Certainly, for lower metallicity smaller deviations are expected. However, one can conclude that the nonequilibrium effects are significant and it should be taken into account in the simulations of the IGM state.

### 3.2.2 An example of the ratio of column densities

The ratio of column densities of ion  $i$  of element  $m$  and ion  $j$  of element  $n$  is (Gnat & Sternberg 2007)

$$\frac{N_i^m}{N_j^n} = \frac{A_m x_i(T)}{A_n x_j(T)}, \quad (4)$$

where  $A_m, A_n$  are the abundances of elements  $m$  and  $n$  (relative to H),  $x_i, x_j$  are the fractions of corresponding ionization states. The absence of the hydrogen density dependence provides more general tool for diagnostics of the IGM. Following Gnat & Sternberg (2007) we consider the ratios  $N_{\text{CIV}}/N_{\text{OVI}}$  and  $N_{\text{NV}}/N_{\text{OVI}}$ .

Figure 11 shows these ratios for power-law spectrum with  $\alpha = 1.7$  and two fluxes  $J_{21} = 0.1$  and  $0.01$  in photoequilibrium and photo-nonequilibrium. The "cooling tracks" are the gray diagrams, where the gray gradation corresponds to gas temperature. As can be expected, the strong difference between the photoequilibrium and time-dependent tracks is seen for  $J_{21} = 0.01$ , whereas the tracks for  $J_{21} = 0.1$  become closer. Indeed, the ionic ratios in a gas exposed to strong ionizing radiation significantly differ from the ratios in collisionally controlled gas (see e.g. Figure 10). The decrease of ionizing flux increases the role of collisions and leads to the transition between photoionized and collisional plasma. However, as one can see in Figures 7 and 9-10 there is no sharp transition between photoionized and collisional plasma. So ionic ratios observed in an object can be satisfied by both photoionized and collisional time-dependent conditions, e.g. for  $J_{21} = 0.001$  the ratio,  $R = x(\text{CIII})/x(\text{CIV})$ , demonstrates a negligible difference from the collisional time-dependent ratio (see Figure 10b). But the difference becomes very clear for  $J_{21} = 0.01$  at  $T \lesssim 10^5 \text{ K}$ .

Figure 11 shows the observational data for the high velocity clouds in the Galactic halo (see Table 8 in Fox et al. 2006). Gnat & Sternberg (2007) showed that the column density ratios in the high velocity clouds observed by Fox et al. (2006) can be fitted using the nonequilibrium collisional model. Here we confirm that the nonequilibrium photoionization models can also explain the observed ratios, for a gas with  $n \sim 10^{-4} \text{ cm}^{-3}$  exposed to  $J_{21} = 0.01 - 0.1$  and  $\alpha = 1.7$  in particular. For example, the ionization states of carbon and oxygen for  $J_{21} = 0.01$  can be found in Figure 8. Under such a flux the CIV, NV and OVI fractions are close to these in the collisional time-dependent model, but strongly overionized in comparison with the photoequilibrium ones. More detailed study is out of scope of this paper.

## 4 CONCLUSIONS

In this paper we have presented the nonequilibrium cooling rates and ionization states of gas enriched with heavy elements and photoionized by external ultraviolet/X-ray radiation. We have studied the dependence of cooling rates on the gas density and metallicity, and also by the radiation field (power-law and the extragalactic background spectra obtained by Haardt & Madau 2001). The calculations are done for a wide range of physical parameters:  $10^4 - 10^8 \text{ K}$  in the gas temperature,  $Z = 10^{-3} - 1 Z_{\odot}$  in the metallicity. For the power-law spectrum, the spectral index  $\alpha$  is taken equal to 1, 1.7 and 5, and for the extragalactic background spectra the redshift varies from 0 to 6. In all calculations, we assume that the gas is optically thin. We have found the following.

- The time-dependent cooling rates depend significantly



on the gas metallicity and density as well as on the flux and shape of the ionizing radiation.

- The time-dependent cooling rates and ionic composition of gas differ strongly from those in the photoequilibrium due to the overionization of ionic states in the time-dependent case. The time-dependent cooling efficiency is generally lower than that in the photoequilibrium, and the nonequilibrium effects can be clearly seen at  $T \lesssim 10^6$  K for the solar metallicity.

- The difference between the time-dependent and equilibrium rates can be significant, its magnitude is maximal at ionization parameter as low as  $\log U \lesssim -5$ , and similar to the difference between the equilibrium and the nonequilibrium cooling rates in the collisionally controlled gas (see Figures 7–9).

- Contributions by individual chemical elements to the total cooling rate can be significantly different for time-dependent and equilibrium plasma at  $T \lesssim 10^6$  K.

- The mismatch of both ionic states and their ratios in the photoequilibrium and photo-nonequilibrium can reach a factor of several.

In this paper we have considered the external radiation and gas parameters, under which the cooling rates and ionic composition in the photoequilibrium and photo-nonequilibrium are expected to be close to each other, and a change of the parameters which violates this equality. The parameter space where the nonequilibrium effects are significant is quite wide. Because the difference between the photoequilibrium and the nonequilibrium is maximal for the ionization parameter  $\log U \lesssim -5$ , then the nonequilibrium collisional cooling rates and ionization states are a better choice for such a low ionization parameter. We have found that the difference decreases with the ionization parameter growth, and the photoequilibrium is reached for ionization parameter as high as  $\log U \gtrsim -2$  for  $Z \lesssim 10^{-2} Z_\odot$  and  $\log U \gtrsim 0$  for  $Z \sim Z_\odot$  (see Table 3). For supersolar metallicity the photoequilibrium is expected to reach for higher ionization parameter. We have concluded that the nonequilibrium photoionization calculations should be conducted, when the contribution from collisions to the total ionization rate is significant. The main reason of the deviation in the time-dependent case is the recombination lag, so the ionic states are expected to be overionized, especially this is notable for metals. Therefore we should pay attention on the importance of use nonequilibrium cooling rates for near-solar (and above) metallicity of gas exposed to arbitrary ionizing radiation flux. Thus, the nonequilibrium cooling rates are the necessary component for study metals in the IGM, mixing metal processes, damped Lyman- $\alpha$  systems, galactic superwinds and so on. Also to simulate correctly the WHIGM ionic composition we need nonequilibrium processes and more exact models for ionizing background flux.

## 5 ACKNOWLEDGEMENTS

The anonymous referee is acknowledged for valuable comments and criticism. The author is grateful to: Yuri Shchekinov for help and many useful discussions; Enn Saar, Sviatoslav Dedikov, Eugene Kurbatov, Eugene Matvienko, Alexei Shaginyan and Eduard Vorobyov for discussions,

their help and advices. Gary Ferland and CLOUDY community are acknowledged for creating of the excellent tool for study of the photoionized plasma – CLOUDY code. This work is supported by the RFBR (project codes 08-02-91321, 09-02-90726, 09-02-00933, 10-02-90705 and 11-02-90701), by the Federal Agency of Education (project code RNP 2.1.1/1937) and by the Federal Agency of Science and Innovations (project 02.740.11.0247). The author acknowledges the Special Astrophysical Observatory RAS and the Institute of Astronomy RAS for hospitality, where he was a visiting scientist.

## REFERENCES

- Agafonova I. I., Levshakov S. A., Reimers D., Fechner C., Tytler D., Simcoe R. A., & Songaila A., 2007, *A&A*, 461, 893
- Altun Z., Yumak A., Badnell N. R., Colgan J., & Pindzola M. S., 2004, *A&A*, 420, 775 (erratum 433, 395 [2005])
- Altun Z., Yumak A., Badnell N. R., Loch S. D., & Pindzola M. S., 2006, *A&A*, 447, 1165
- Arnaud M. & Rothenflug R., 1985, *A&AS*, 60, 425
- Arnaud M. & Raymond J., 1992, *ApJ*, 398, 394
- Asplund, M., Grevesse, N., & Sauval, A. J. 2005, in *ASP Conf. Ser. 336, Cosmic Abundances as Records of Stellar Evolution and Nucleosynthesis*, ed. T. G. Barnes III & F. N. Bash (San Francisco: ASP), 25
- Badnell N. R., 2006a, *Atomic and Molecular Diagnostic Processes in Plasmas* (Dept. Physics, Univ. Strathclyde), <http://amdpp.phys.strath.ac.uk/tamoc/RR/>
- Badnell N. R. 2006b, *Atomic and Molecular Diagnostic Processes in Plasmas* (Dept. Physics, Univ. Strathclyde), <http://amdpp.phys.strath.ac.uk/tamoc/DR/>
- Badnell N. R. 2006c, *A&A*, 447, 389
- Bautista M. A. & Badnell N. R. 2007, *A&A*, 466, 755
- Benjamin R. A., Benson B. A. & Cox D. P., 2001, *ApJ*, 554, L225
- Böhringer H. & Hensler G., 1989, *A&A*, 215, 147
- Bregman J.N., Canizares C. R., Cen R., de Herder J-W., Bonamente M. et al. , 2009, *Astro2010: The Astronomy and Astrophysics Decadal Survey*, Science White Papers, no. 24, arXiv:0906.4984
- Brown P. N., Byrne G. D., & Hindmarsh A. C., 1989, *SIAM J. Sci. Stat. Comput.*, 10, 1038
- Bryans P., Badnell N. R., Gorczyca T. W., Laming J. M., Mitthumsiri W., Savin D. W., 2006, *ApJS*, 167, 343
- Cen R. & Fang T., 2006, *ApJ*, 650, 573
- Cen R. & Ostriker J.P., 1999, *ApJ*, 514, 1
- Colgan J., Pindzola M. S., Whiteford A. D. & Badnell N. R. 2003, *A&A*, 412, 597
- Colgan J., Pindzola M. S. & Badnell N. R. 2004, *A&A*, 417, 1183 (erratum 429, 369 [2005] )
- Cox D. P., & Tucker W. H. 1969, *ApJ*, 157, 1157
- Crain R. A., Theuns T., Dalla Vecchia C., Eke V. R., Frenk C. S. et al. , 2009, *MNRAS* 399, 1773
- Danforth C.W. & Shull J.M., 2008, *ApJ*, 679, 194
- Davé R., Cen R., Ostriker J.P., et al. , 2001, *ApJ*, 552, 473
- de Avillez M. A. & Breitschwerdt D., 2010, *Highlights of Astronomy*, Vol. 15, 468, arXiv:0910.2216
- de Avillez M. A. & Breitschwerdt D., 2010, *ASP Conf. Ser.* in press, arXiv:1010.5654



- Drake J. J. & Testa P., 2005, *Nature*, 436, 525
- Edgar R. J. & Chevalier R. A., 1986, *ApJ*, 310, L27
- Efstathiou G., 1992, *MNRAS*, 256, 43
- Faucher-Giguère C.-A., Lidz A., Zaldarriaga M., Hernquist L., 2009, *ApJ* 703, 1416
- Ferland G. J., Korista K. T., Verner D. A., Ferguson J. W., Kingdon J. B. & Verner E. M. 1998, *PASP*, 110, 761
- Ferrara A., Scannapieco E., Bergeron J., 2005, *ApJL*, 634, 37
- Fox A. J., Wakker B. P., Savage B. D., Tripp T. M., Sembach K. R., Bland-Hawthorn J., 2005, *ApJ*, 630, 332
- Fukugita M. & Peebles P. J. E., 2004, *ApJ*, 616, 643
- Gaetz T. J. & Salpeter E. E., 1983, *ApJS*, 52, 155
- Gnat O. & Sternberg A., 2004, *ApJ*, 608, 229
- Gnat O. & Sternberg A., 2007, *ApJS*, 168, 213
- Gnat O. & Sternberg A., 2009, *ApJ*, 693, 1514
- Haardt F. & Madau P., 1996, *ApJ*, 461, 20
- Haardt F. & Madau P., 2001, in *Clusters of Galaxies and the High Redshift Universe Observed in X-rays*, ed. D. M. Neumann & J. T. V. Tran, astro-ph/0106018 (HM01)
- House L. L., 1964, *ApJS*, 8, 307
- Hughes J. P. & Singh K. P., 1994, *ApJ*, 422, 126
- Kaastra J.S. & Mewe R., 1993, *A&AS*, 97, 443
- Kafatos M., 1973, *ApJ*, 182, 433
- Kingdon J. B. & Ferland G. J., 1996, *ApJS*, 106, 205
- Kitayama T., Susa H., Umemura M., Ikeuchi S., 2001, *MNRAS*, 326, 1353
- Landi E. & Landini M., 1999, *A&A*, 347, 401
- Madau P., Ferguson H. C., Dickinson M. E., Giavalisco M., Steidel Ch. C., Fruchter A., 1996, *MNRAS*, 283, 1388
- Madau P. & Haardt F., 2009, *ApJL*, 693, 100
- Mazzotta P., Mazzitelli G., Colafrancesco S., & Vittorio N., 1998, *Astron. Astrophys. Suppl. Ser.* 133, 403
- Miniati F., Ferrara A., White S. D. M., Bianchi S. 2004, *MNRAS*, 348, 964
- Mitnik D. M. & Badnell N. R. 2004, *A&A*, 425, 1153
- Nicastro F., et al. 2005, *Nature*, 433, 495
- Pettini M, 1999, in the *Proceedings of the ESO Workshop ‘Chemical Evolution from Zero to High Redshift’*. Eds. J. R. Walsh, M. R. Rosa. Berlin: Springer-Verlag, p. 233
- Raga A. C., Mellema G., Lundqvist P., 1997, *ApJS*, 109, 517
- Raymond J. C., Cox D. P. & Smith B. W. 1976, *ApJ*, 204, 290
- Sazonov S. Yu., Ostriker J. P., Sunyaev R. A., 2004, *MNRAS*, 347, 144
- Schaye J., Aguirre A., Kim T., Theuns T., Rauch M., Sargent W.L.W., 2003, *ApJ*, 596, 768
- Scott J. E., Kriss G. A., Brotherton M., Green R. F., Hutchings J., Shull J. M., & Zheng W., 2004, *ApJ*, 615, 135
- Schmutzler T. & Tscharnuter W. M., 1993, *A&A*, 273, 318
- Shapiro P. R. & Moore R. T., 1976, *ApJ*, 207, 460
- Shull J. M. & van Steenberg M., 1982, *ApJS*, 48, 95
- Simcoe R.A., Sargent W.L.W., Rauch M., Becker G., 2006, *ApJ*, 637, 648
- Sutherland R. S. & Dopita M. A., 1993, *ApJS*, 88, 253
- Telfer R. C., Zheng W., Kriss G. A., & Davidsen A. F., 2002, *ApJ*, 565, 773
- Vasiliev E. O., Sethi S. K., Nath B. B., 2010, *ApJ*, 719, 1343
- Verner D. A., Ferland G. J., Korista K. T. & Yakovlev D.G., 1996, *ApJ*, 465, 487
- Verner D. A., & Yakovlev D.G., 1995, *A&AS*, 109, 125
- Voronov G. S., 1997, *At. Data Nucl. Data Tables*, 65, 1
- Wiersma R., Schaye J., Smith B.D., 2009, *MNRAS*, 393, 99
- Yoshikawa K. & Sasaki S., 2006, *PASJ*, 58, 641
- Zatsarinny O., Gorczyca T. W., Korista K. T., Badnell N. R., & Savin D. W., 2003, *A&A*, 412, 587 (erratum 438, 743 [2005])
- Zatsarinny O., Gorczyca T. W., Korista K. T., Badnell N. R., & Savin D. W., 2004a, *A&A*, 417, 1173 (erratum 440, 1203 [2005])
- Zatsarinny O., Gorczyca T. W., Korista K. T., Badnell N. R., & Savin D. W., 2004b, *A&A*, 426, 699
- Zatsarinny O., Gorczyca T. W., Fu J., Korista K. T., Badnell N. R., & Savin D. W., 2006, *A&A*, 447, 379
- Zheng W., Kriss G. A., Telfer R. C., Grimes J. P., & Davidsen A. F., 1997, *ApJ*, 475, 469